Controlled Chelation between Tannic Acid and Fe Precursors to Obtain N, S Co-doped Carbon with High Density Fe-Single Atom-Nanoclusters for Highly Efficient Oxygen Reduction Reaction in Zn-Air Battery

Hong Li,[a] Kai Du,[c] Chensheng Xiang,[c] Pengfei An,[f] Xinxin Shu,[e] Yaru Dang,[g] Chenshuo Wu,[a] Jin Wang,[a] Wei Du,[b] Jintao Zhang,[e] Shenggang Li,[g] He Tian,*[c] Shuangyin Wang,*[d] and Haibing Xia*[a]

[a]State Key Laboratory of Crystal Materials, Shandong University, Jinan, 250100, P. R China; E-mail: hbxia@sdu.edu.cn
[b]School of Environment and Material Engineering, Yantai University, Yantai 264005, Shandong, China;
[c]Center of Electron Microscope, State Key Laboratory of Silicon Materials, School of Materials Science and Engineering, Zhejiang University, Hangzhou, 310027, P. R China. E-mail: hetian@zju.edu.cn
[d]State Key Lab of Chemo/Bio-Sensing and Chemometrics, Provincial Hunan Key Laboratory for Graphene Materials and Devices, College of Chemistry and Chemical Engineering, Hunan University, Changsha, 410082, P. R. China. E-mail: shuangyinwang@hnu.edu.cn
[e]School of Chemistry and Chemical Engineering, Shandong University, Jinan, 250100, P. R China;
[f]Beijing Synchrotron Radiation Facility, Institute of High Energy Physics, Chinese Academy of Sciences , Beijing, 100049, P. R .China;
[g]Low-Carbon Conversion Center, Shanghai Advanced Research Institute, Chinese Academy of Sciences, 100 Haike Road, Shanghai, 201210, P. R .China.

Fig. S1 Digital photographs of pure PANI polymer (a), PANI–TA (b), PANI-Fe (c), PANI-TA-Fe (d).
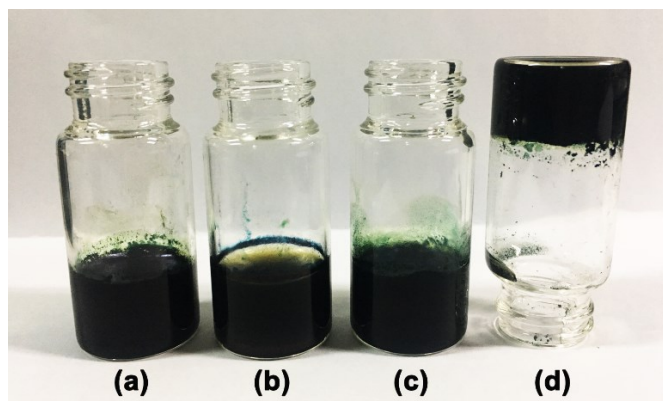
Fig. S2 Complexation of tannic acid (TA) molecules with Fe^{3+} ions at pH < 3. The molar ratio of Fe precursor to TA can be adjusted from 0 to 10.
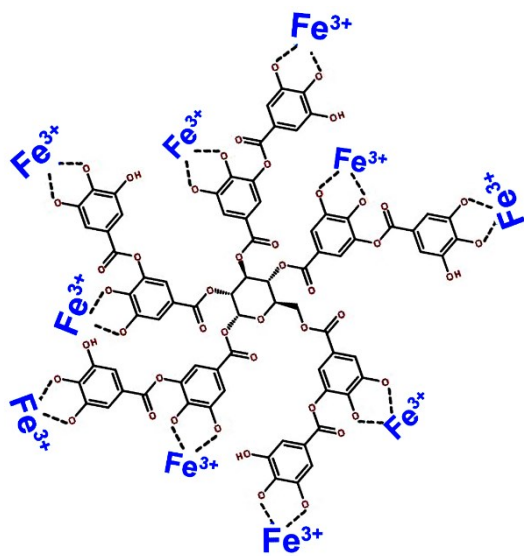
Fig. S3 (A) LSV curves and (B) half-wave potentials of the resulting N, S co-doped $C_{PANI-TA-Fe}$ Fe catalysts at fixed concentration of Fe precursor: (a) TA: Fe =0.06:1, (b) TA: Fe = 0.1:1, (c) TA: Fe =0.3:1, and (d) Fe: TA=0.6:1. The concentration of Fe precursor is 0.48 mM.
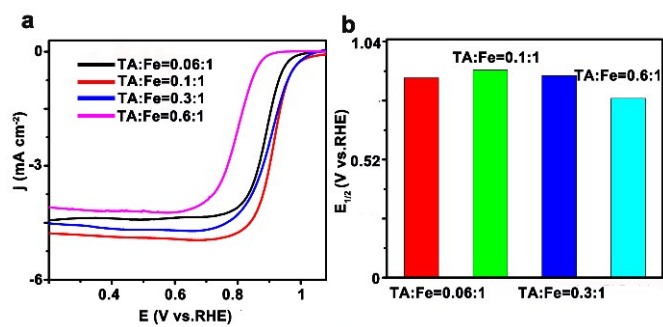
Fig. S4 (A) LSV curves and (B) half-wave potentials of the resulting N, S co-doped $C_{PANI-TA-Fe}$ Fe catalysts at fixed concentration of TA: (a) Fe: TA = 5:1 (b) Fe: TA = 8:1, (c) Fe: TA =10:1, and (d) Fe: TA =15:1. The concentration of TA precursor is 0.048 mM.
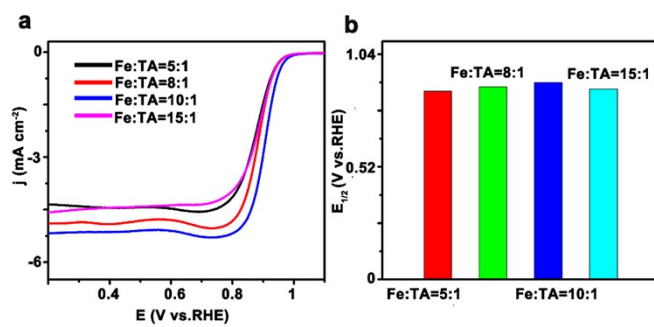
Fig. S5 (a) LSV curves and (b) half-wave potentials of the resulting N, S co-doped C$_{PANI-TA-Fe}$ Fe-SA-NC catalysts obtained at different pyrolysis temperatures. The concentrations of TA and Fe precursor are 0.04 mM and 0.5 mM, respectively.
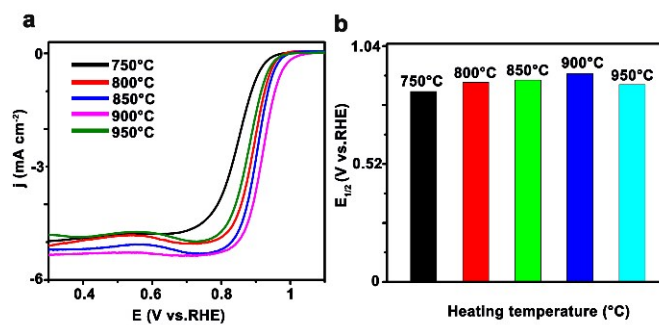
Fig. S6 (a) LSV curves and (b) half-wave potentials of the resulting N, S co-doped $C_{PANI-TA-Fe}$ Fe-SA-NC catalysts obtained at different heating rates. The concentrations of TA and Fe precursor are 0.04 mM and 0.5 mM, respectively.
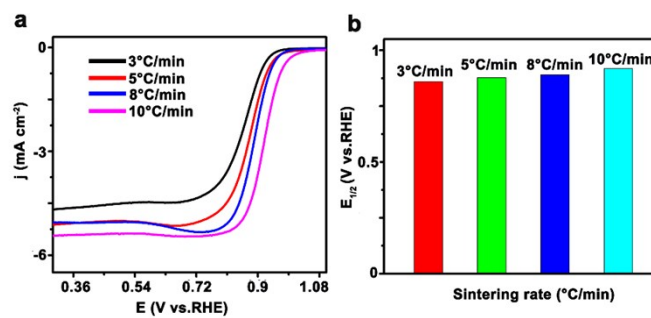
Fig. S7 HAADF-STEM-EDS mapping images of the elemental distributions of Fe in the N, S co-doped $C_{PANI-TA-Fe}$ Fe-SA-NC catalysts after acid treatment of different times: (a, b) 4h, and (c, d) 8h.
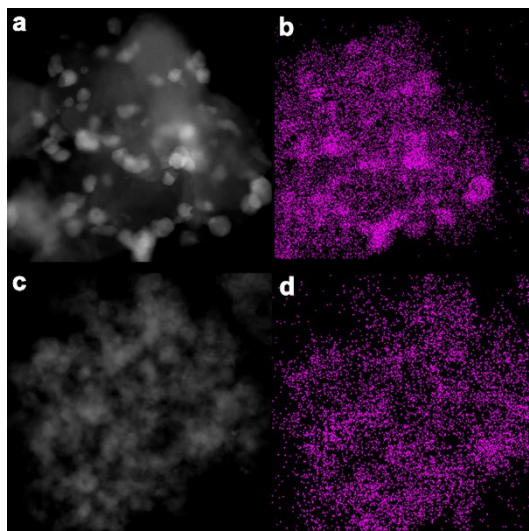
After the acid treatment of 8 hours, unstable Fe-NPs in the N, S co-doped $C_{PANI-TA-Fe}$ Fe-SA-NC catalysts were almost removed (shown as in Fig. S7).

Fig. S8 LSV curve of N, S co-doped C$_{PANI-TA-Fe}$ Fe-SA-NC catalysts after the acid treatment of different times, measured in O$_2$-saturated 0.1 M KOH solution at a scan rate of 5 mV s^{-1} and at a speed of 1,600 rpm.
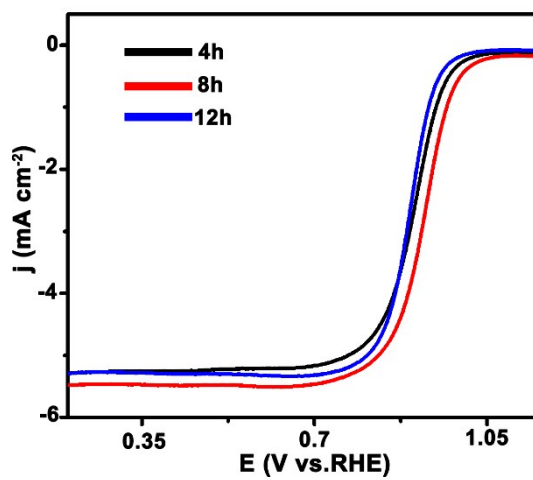
Fig. S9 TEM images of as-prepared (a) 3D PANI network, (b) 3D PANI-TA network, (c) 3D PANI-Fe network, and (d) PANI-TA-Fe hydrogel; and their corresponding products (e to h) after pyrolysis: (e) N, S co-doped C_{PANI}, (f) N, S co-doped $C_{PANI-TA}$, (g) N, S co-doped $C_{PANI-Fe}$ Fe-NP and (h) N, S co-doped $C_{PANI-TA-Fe}$ Fe-SA-NC catalysts; High magnification TEM images showing the edges (i) of N, S co-doped C_{PANI}, (j) N, S co-doped $C_{PANI-TA}$, (k) N, S co-doped $C_{PANI-Fe}$ Fe-NP and (l) N, S co-doped $C_{PANI-TA-Fe}$ Fe-SA-NC catalysts, respectively.
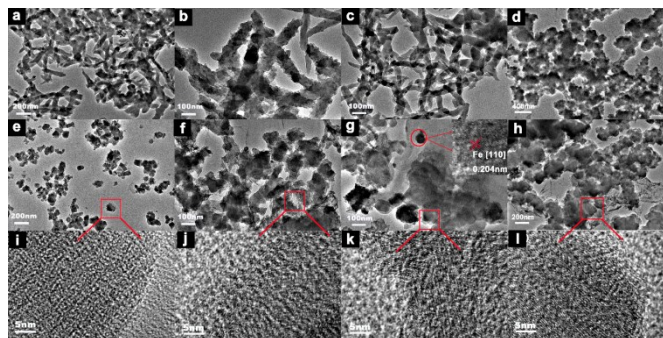
In the absence of Fe^{3+} ions or TA, the morphology of PANI polymer formed in the solution during the preparation of the N, S co-doped C_{PANI} catalysts, and N, S co-doped $C_{PANI-TA}$ catalysts and N, S co-doped $C_{PANI-Fe}$ Fe-NP catalysts were nanofibers. In addition, these PANI nanofibers would disappear after the pyrolysis. However, when TA and Fe^{3+} coexist, a dark green hydrogel of PANI polymer were obtained, in which PANI polymer were not in nanofiber format.

Fig. S10 (a) TEM and (b) HRTEM images of N, S co-doped $C_{PANI-TA}$ catalysts.
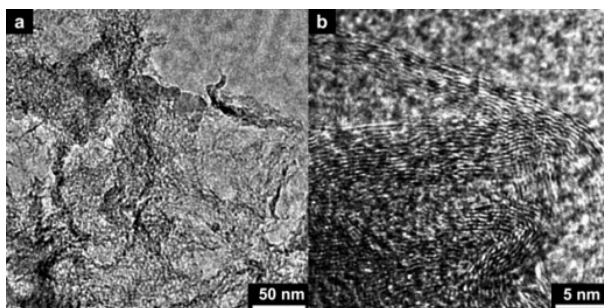
As shown in Fig. S10a, there is a small amount of graphene-like flake-carbon materials, besides the presence of a large amount of bulk carbon (Fig. S9e and S9f). In addition, these graphene-like flake-carbon materials show obvious lattice fringes (Fig. S10b). Thus, the formation of graphene-like flake-carbon materials enhance the total graphitization degree of N, S co-doped $C_{PANI-TA}$ catalysts, compared with N, S co-doped C_{PANI} catalysts. Considering the molecular structure of TA, graphene-like flake-carbon materials may result from TA molecules. Thus, the presence of TA may enhance the total graphitization degree of N, S co-doped $C_{PANI-TA}$ catalysts after the pyrolysis, in comparison with N, S co-doped C_{PANI} catalysts.

Fig. S11 (A) HAADF-STEM image of N, S co-doped $C_{PANI-TA-Fe}$ Fe-SA-NC catalysts, enlarged image of Fe-SA-NCs (B) and Fe-SAs (C), which are labelled with red circles. (D) The histogram of size distribution of the Fe-SA-NCs.
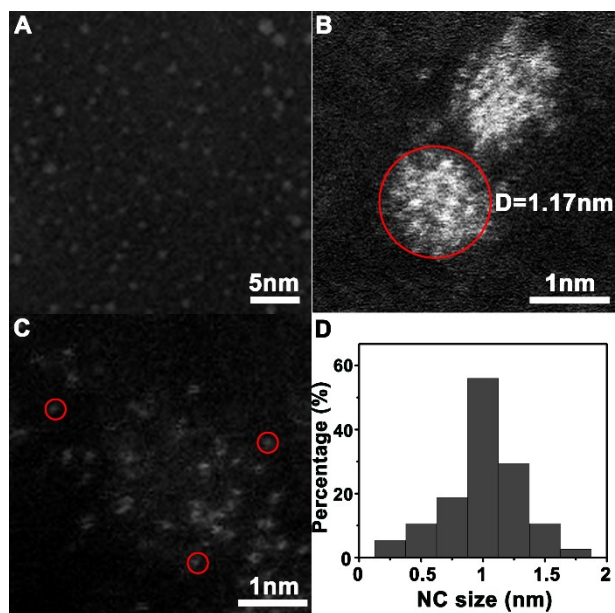
Fig. S12 HAADF-STEM image of Fe-SA-NCs with sizes smaller than 1.5 nm (A), Fe-SA-NCs with bigger than 1.5 nm (B), 3.8 nm Fe NPs (C), (D) Schematic representations of the distribution and the lattice distance of Fe atoms in Fe-SA-NCs (D-a and D-c), and Fe NPs (D-b and D-d) and (E) Schematic models of the possible local atomic configuration around Fe atoms in N, S co-doped $C_{PANI-TA-Fe}$ Fe-SA catalysts (a), N, S co-doped $C_{PANI-TA-Fe}$ Fe-SA-NC catalysts with sizes smaller than 1.5 nm (b), N, S co-doped $C_{PANI-TA-Fe}$ Fe-SA-NC catalysts with sizes bigger than 1.5 nm (c) and N, S co-doped $C_{PANI-TA-Fe}$ Fe-NP catalysts with sizes of about 3.8 nm.
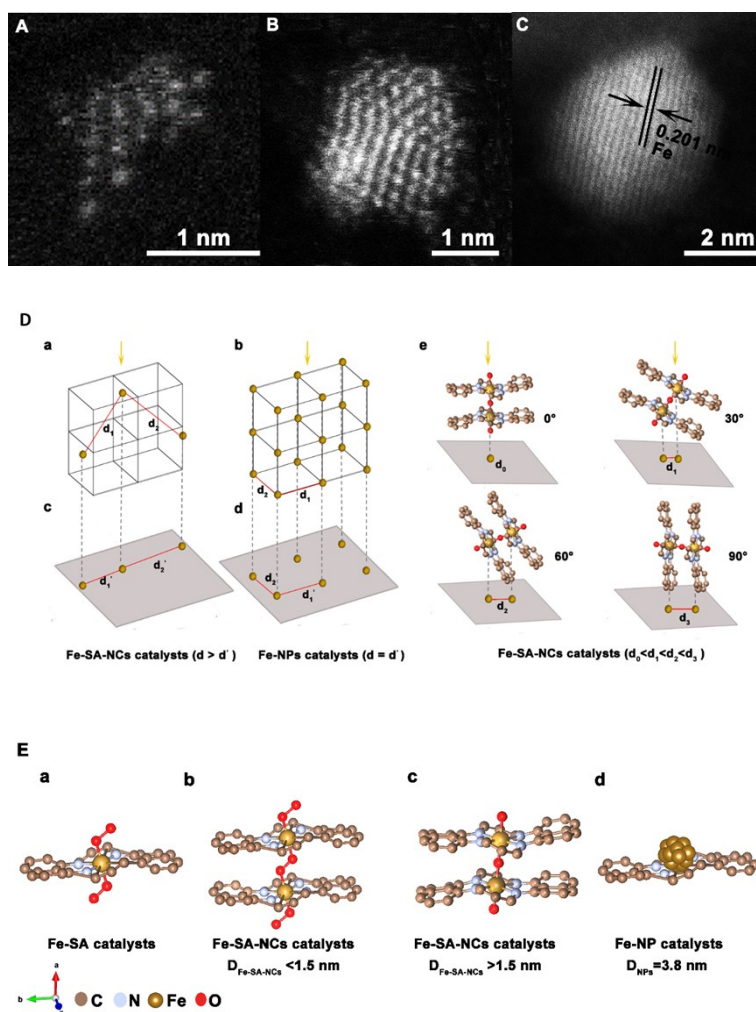
It can be clearly seen that with the increasing size of Fe species (or Fe atoms), the distances between Fe atoms gradually decrease. Moreover, the arrangement of Fe atoms gradually becomes from disorder (Fig. S12A) to distorted lattice orientation (Fig. S12B), and well-aligned lattice orientation (Fig. S12C). The results indicate that almost of Fe atoms in Fe-SA-NCs with sizes smaller than 1.5 nm are distributed randomly (Fig. S12A) and a small fraction of Fe atoms in Fe-SA-NCs with sizes bigger than 1.5 nm form the distorted crystal lattices (Fig. S12B). In comparison with Fe NPs, the real distance between them cannot be estimated by lattice distance because these Fe atoms are randomly distributed in the three-dimensional space and not in the same lattice plane. Accordingly, the different projection images of these Fe atoms in the Fe-SA-NCs would result in the different types of distances between Fe atoms (Fig. S12D-a, S12D-c and S12D-e). As for Fe NPs, the uniform lattice distance are observed due to the perfect single-crystalline structure (Fig. S12D-b and S12D-d). Furthermore, the typical distances among Fe atoms in Fe NCs with sizes

smaller than 1.5 nm and Fe NCs with bigger than 1.5 nm both are larger than those in 3.8 nm Fe NPs.

In our work, the formation of Fe-SA, Fe-SA-NC and Fe-NPs were achieved by controlling the molar ratio of Fe-to-TA, in which the source of the oxygen atoms mainly result from TA. When the molar ratio of Fe-to-TA is less than 10, Fe-SAs would be dominant and the model of the possible local atomic configuration around Fe atoms is shown in Fig. S12E-a. With the increasing amount of Fe precursor, the relative ratio of oxygen between Fe atoms would become fewer and the distances among Fe atoms in the Fe species would become close (Fig. S12E-b, S12E-c and S12E-d). For instance, the distances between Fe atoms in the Fe NCs with sizes bigger than 1.5 nm become close because the oxygen atom would possibly become from 2 to1 between two Fe atoms(Fig. S12E-b and S12E-c), on the basis of the simulation result.

Fig. S13 (A) Schematic models (a and b), TEM image (c), and HAADF-STEM image (d) of N, S co-doped $C_{PANI-TA-Fe}$ Fe-NP catalysts, which were obtained when the TA-to-Fe molar ratio is 1:13. (B) Schematic models (c and d), TEM image (g), and atomic resolution HAADF-STEM image (h) of N, S co-doped $C_{PANI-TA-Fe}$ Fe-SA catalysts, which were obtained when the TA-to-Fe molar ratio is 1:2.
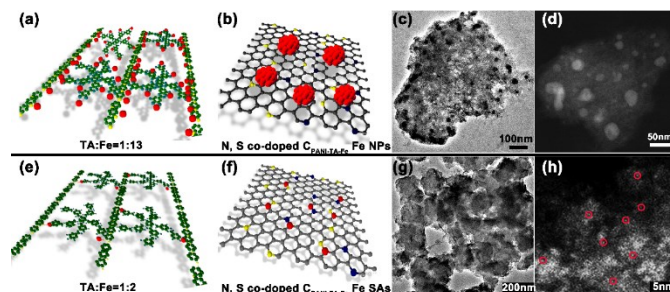
Due to the protection of carbon layer on their surfaces, the Fe NPs in N, S co-doped $C_{PANI-Fe}$ Fe-NP catalysts and N, S co-doped $C_{PANI-TA-Fe}$ Fe-NP catalysts would not dissolve after the short-time acid treatment (8h).

Fig. S14 Energy Dispersive Spectrometer (EDS) analysis of N, S co-doped C$_{PANI-TA-Fe}$ Fe-SA-NC catalysts.
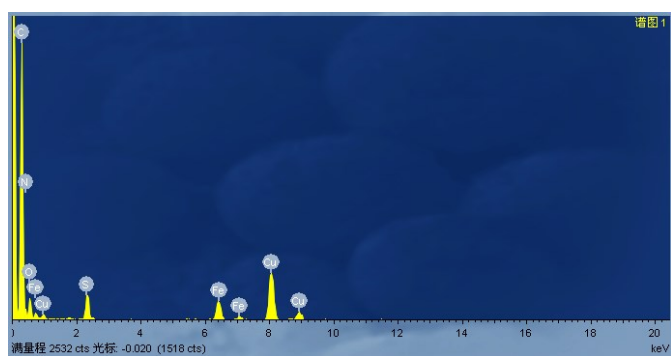
Fig. S15 N$_2$ sorption isotherms (a, c and e) and the corresponding pore size distributions (b, d, and f) of N, S co-doped C$_{PANI}$ (a and b), N, S co-doped C$_{PANI-TA}$ (c and d) and N, S co-doped C$_{PANI-Fe}$ Fe-NP catalysts (e and f).
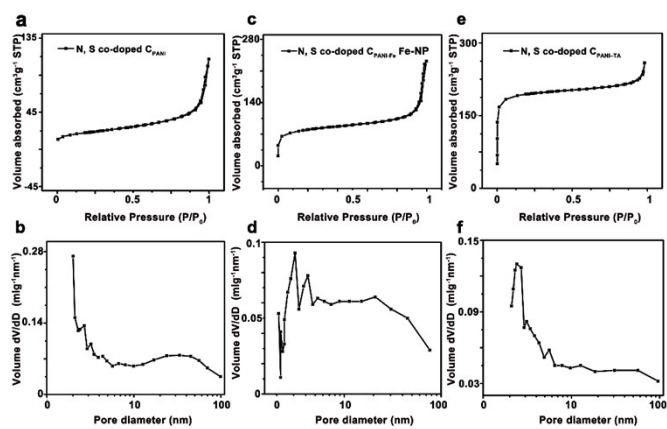
Fig. S16 XPS survey full scan (A), high-resolution (B) N 1s, and Fe 2p spectra (C) of N, S co-doped $C_{PANI-Fe}$ Fe-NP catalysts.
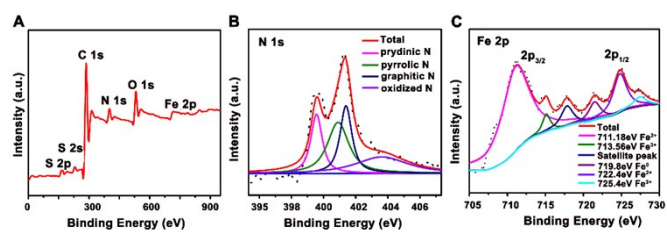
Fig. S17 High-resolution C 1s of the N, S co-doped C$_{PANI-TA-Fe}$ Fe-NP catalysts (A) and N, S co-doped C$_{PANI-TA-Fe}$ Fe-SA-NC catalysts (B).
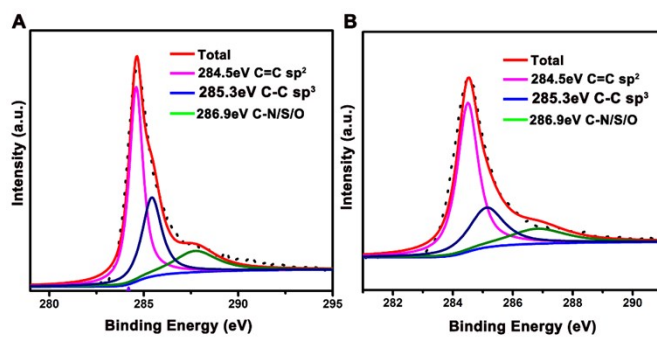
Fig. S18 Fourier-transformed EXAFS data of Fe atoms in N, S co-doped $C_{PANI-TA-Fe}$ Fe-SA-NC catalysts, N, S co-doped $C_{PANI-TA-Fe}$ Fe-NP catalysts with sizes of about 3.8 nm Fe NPs and Fe_2O_3 (as the reference).
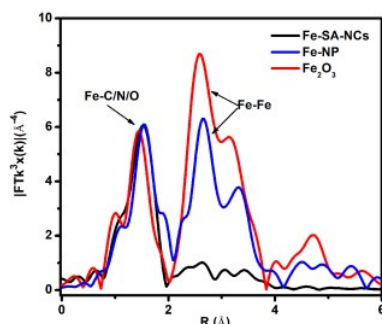
As shown in the Fig. S18, the Fourier transforms of Fe K EXAFS spectrum of N, S co-doped $C_{PANI-TA-Fe}$ Fe-NP catalysts with sizes of about 3.8 nm Fe NPs exhibits two peaks at 1.52 Å and at about 2.6 Å(without phase shift correction), which are attributed to Fe-N/C/O scattering paths, and the peak of Fe-Fe bonds,[1,2] respectively. The presence of the peak of Fe-Fe bonds indicate that as the Fe content used for synthesis of N, S co-doped $C_{PANI-TA-Fe}$ Fe-based catalysts increases, the distance between Fe atoms becomes so close that Fe-Fe bond can be formed in the N, S co-doped $C_{PANI-TA-Fe}$ Fe-NP catalysts with sizes of about 3.8 nm Fe NPs (Fig. S12E in ESI†). Accordingly, an obvious peak of Fe-Fe bond is observed in further distance (the second shell). Thus, the absence of the peak of Fe-Fe bonds in the EXAFS spectrum of N, S co-doped $C_{PANI-TA-Fe}$ Fe-SA-NC catalysts indicates that Fe-SA-NCs are different from Fe NPs in the carbon materials.

Fig. S19 CV curves of N, S co-doped C_{PANI} catalysts (a), N, S co-doped $C_{PANI-TA}$ catalysts (b) and N, S co-doped $C_{PANI-Fe}$ Fe-NP catalysts (c) in O_2-saturated 0.1 M KOH electrolyte.
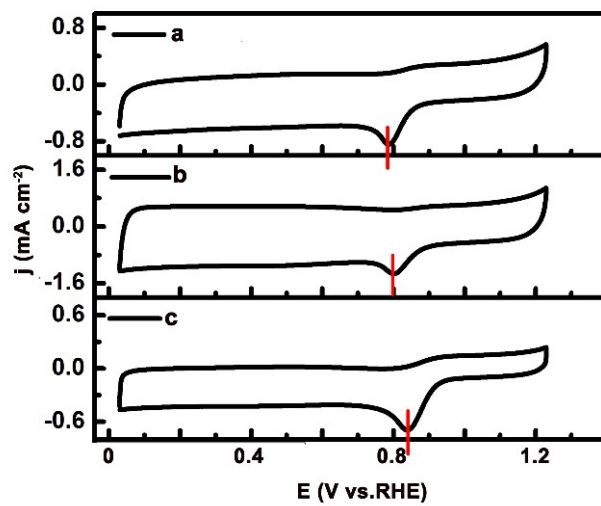
Fig. S20 LSVs curves at various rotation rates and the corresponding K-L plots (j^{-1} vs. $\omega^{-1/2}$) at different potentials of N, S co-doped C_{PANI} catalysts (A and B), N, S co-doped $C_{PANI-TA}$ catalysts (C and D), N, S co-doped $C_{PANI-Fe}$ Fe-NP catalysts (E and F)and commercial Pt/C catalysts (G and H). The tests (A, C, E, and G) were investigated at scan rate 5 mV s^{-1} in O_2-saturated 0.1 M KOH.
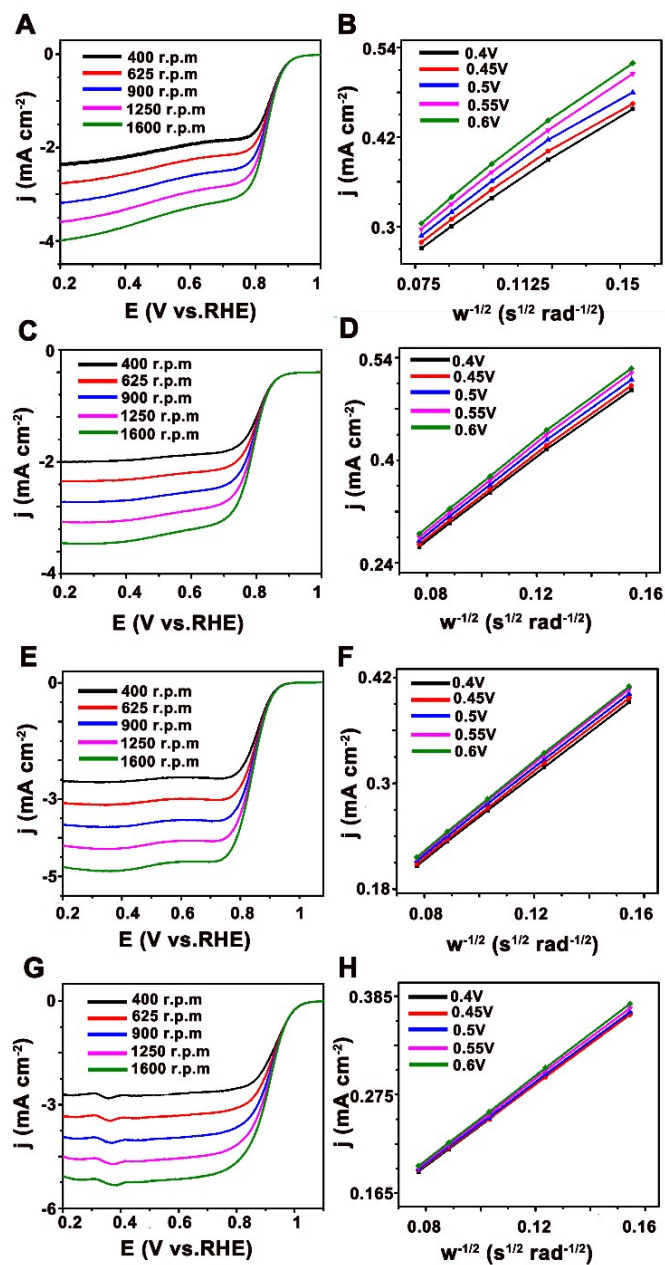
Fig. S21 The electron transfer number at different potentials of N, S co-doped C_{PANI} (a), N, S co-doped $C_{PANI-TA}$ (b), N, S co-doped $C_{PANI-Fe}$ Fe-NP catalysts (c), N, S co-doped $C_{PANI-TA-Fe}$ Fe-SA-NC catalysts (d), and commercial Pt/C catalysts (e).
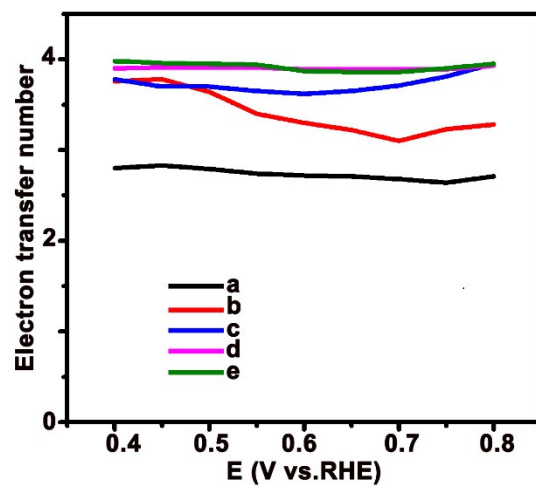
Fig. S22 LSVs curves at various rotation rates of N, S co-doped $C_{PANI-TA-Fe}$ Fe-SA-NC catalysts with the loading of the elemental Fe (about 0.056 mg$_{Fe}$ cm^{-2}). The tests were investigated at scan rate 5 mV s^{-1} in O_2-saturated 0.1 M KOH. The inset is the corresponding K-L plots (j^{-1} vs. $\omega^{-1/2}$) at 0.9V.
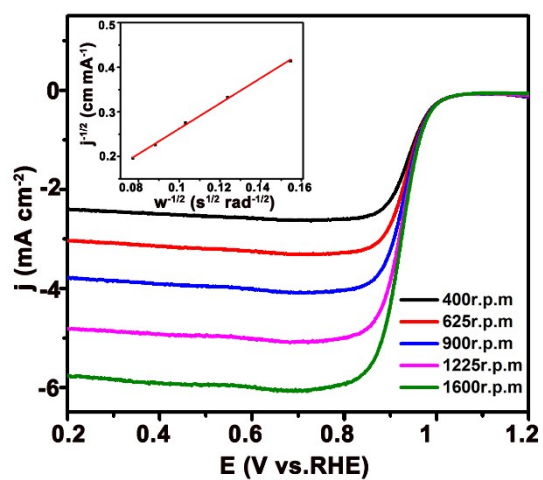
Fig. S23 LSV curves of N, S co-doped C$_{PANI-TA-Fe}$ Fe-SA catalysts (a) and commercial Pt/C catalysts (b) before (black) and after (red) 4000 potential cycles. The ADT teste were performed in the O$_2$-saturated 0.1 M KOH electrolyte at room temperature by applying potential cycling between 1.0 and 0.2 V vs RHE at a sweep rate of 100 mV s^{-1} for 4,000 cycles.
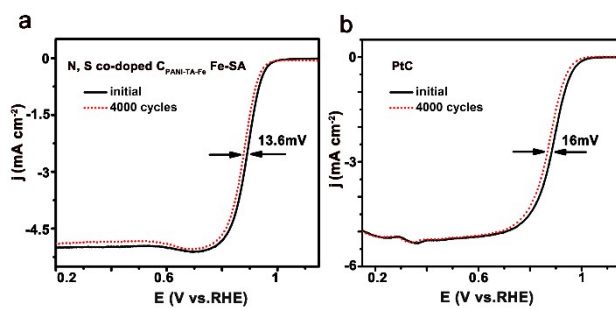
Fig. S24 N$_2$ sorption isotherms(A) and the corresponding pore size distributions (B) of N, S co-doped C$_{PANI-TA-Fe}$ Fe-SA catalysts.
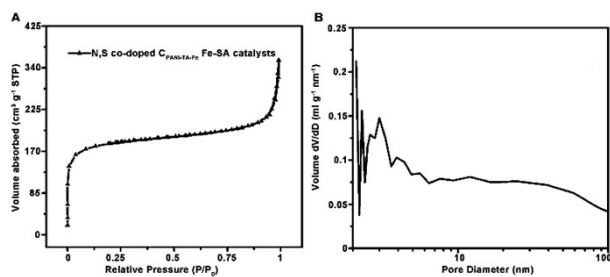
Fig. S25 LSV curves of N, S co-doped $C_{PANI-TA-Fe}$ Fe-NP catalysts (a), N, S co-doped $C_{PANI-TA-Fe}$ Fe-SA catalysts (b), and N, S co-doped $C_{PANI-TA-Fe}$ Fe-SA-NC catalysts (c) on the RDEs in O_2-saturated 0.1 M KOH solution at a scan rate of 5 mV s^{-1} and at a speed of 1,600 rpm.
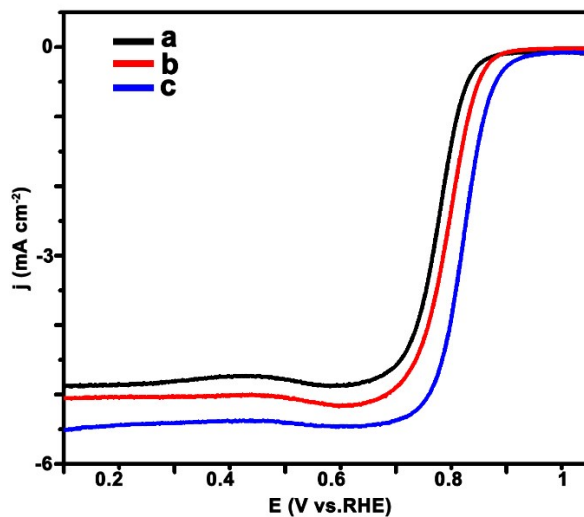
Fig. S26 (A) LSV curves of the resulting N, S co-doped $C_{PANI-TA-Fe}$ Fe-SA-NC-HT2 catalysts obtained at different second heat-treatment temperatures for a hold time of 1 h. (B) The ORR performance of N, S co-doped $C_{PANI-TA-Fe}$ Fe-SA-NC-HT1 catalysts, N, S co-doped $C_{PANI-TA-Fe}$ Fe-SA-NC-HT2 (400°C、1h) catalysts and commercial Pt/C were tested in 0.1 M $HClO_4$ electrolyte. (C) LSVs curves at various rotation rates of N, S co-doped $C_{PANI-TA-Fe}$ Fe-SA-NC-HT2 (400°C、1h) catalysts. (D) Electron transfer number of N, S co-doped $C_{PANI-TA-Fe}$ Fe-SA-NC-HT2 (400°C、1h) catalysts and commercial Pt/C catalysts calculated from the K-L equation. (E) ORR polarization curves before and after 20000 potential cycles of N, S co-doped $C_{PANI-TA-Fe}$ Fe-SA-NC-HT2 (400°C、1h) catalysts. (F) ORR polarization curves before and after 5000 potential cycles of commercial Pt/C.
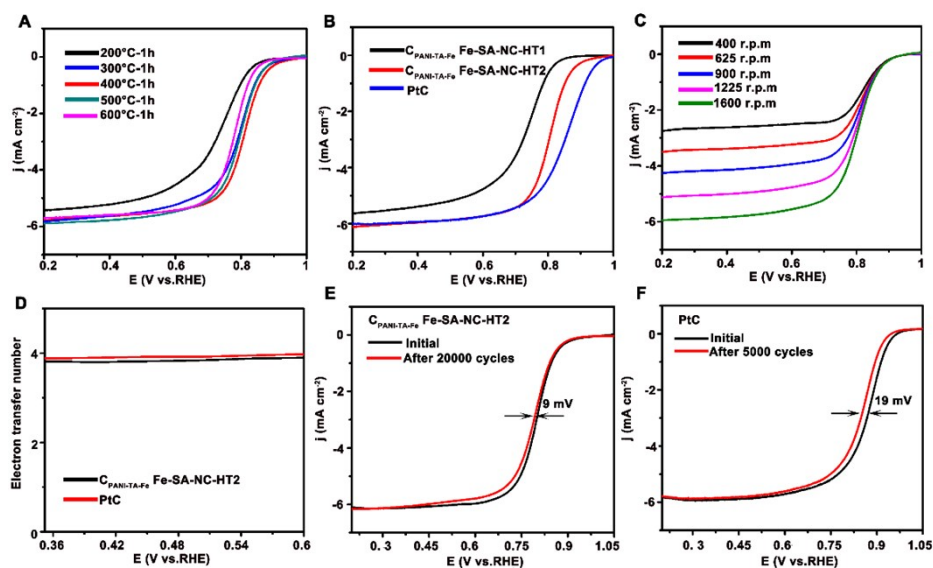
Fig. S27 TEM images of the resulting N, S co-doped C$_{PANI-TA-Fe}$ Fe-SA-NC-HT2 catalysts obtained at different second heat-treatment temperatures for a hold time of 1 h : (a) 200 °C, (b) 300 °C, (c) 400 °C, (d) 500 °C, (e) 600 °C, (f) 700 °C, respectively.
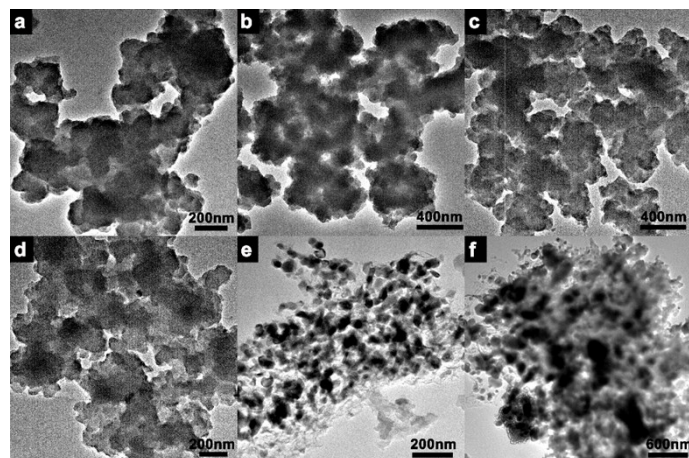
To prepare a transitional metal-incorporated N-doped carbon with excellent properties under acidic conditions, the N, S co-doped C$_{PANI-TA-Fe}$ Fe-SA-NC catalysts is subjected to a re-heat-treatment process in Ar to remove the anions that bound on the surface during the acid-washing.[3-6] As shown in Fig. S25A and S25B, N, S co-doped C$_{PANI-TA-Fe}$ Fe-SA-NC catalysts, which were treated at 400°C for 1h after the first round of heat treatment and the following acid etching (named as N, S co-doped C$_{PANI-TA-Fe}$ Fe-SA-NC-HT2 catalysts), exhibit a half-wave potential of 0.807 V versus RHE, which is positively shifted by nearly 30 mV, in comparison with the N, S co-doped C$_{PANI-TA-Fe}$ Fe-SA-NC-HT1 catalysts. TEM images of N, S co-doped C$_{PANI-TA-Fe}$ Fe-SA-NC-HT2 catalysts indicate that the temperature at this time is much lower than the minimum 600 °C needed to form new catalytic sites from Fe salt, N and C precursors (Fig. S26c). As shown in the Fig. S26e, Fe-NPs are observed on the surface of N, S co-doped C$_{PANI-TA-Fe}$ Fe-SA-NC-HT2 catalysts after a re-heat-treatment in argon above 600 °C. This result further proves that the active sites (Fe-SA-NCs) of N, S co-doped C$_{PANI-TA-Fe}$ Fe-SA-NC-HT2 catalysts are composed of ultra-stable, Fe-SA, which is atomically anchored in the N,S co-doped porous carbon matrix. In addition, the activities of N, S co-doped C$_{PANI-TA-Fe}$ Fe-SA-NC-HT2 catalysts are comparable to the highest reported activities of various types of NPMCs (Table S9).Their electron transfer number was calculated to be 3.8-3.9 in the range of 0.35 V to 0.6 V, indicating that their dominant ORR pathway is still four-electron process in acidic media (Fig. S25C and S25D). The stability of the N, S co-doped C$_{PANI-TA-Fe}$ Fe-SA-NC-HT2 catalysts under acidic conditions is also evaluated by an accelerated degradation test (ADT) in O$_2$-saturated 0.1M HClO$_4$. Strikingly, they only show a 9 mV decay in the E$_{1/2}$ value after 20000 cycles, which is much better than the Pt/C catalysts (19 mV decay after 5000 cycles; Fig. S25E and S25F). All of results mentioned above indicate that N, S co-doped C$_{PANI-TA-Fe}$ Fe-SA-NC-HT2 catalysts also have good prospects for ORR applications under the acidic electrolytes.

Fig. S28 The plot of the open circuits of the N, S co-doped $C_{PANI-TA-Fe}$ Fe-SA-NC catalysts、N, S co-doped $C_{PANI-TA-Fe}$ Fe-SA catalysts and commercial Pt/C catalysts, based rechargeable Zn–air battery.
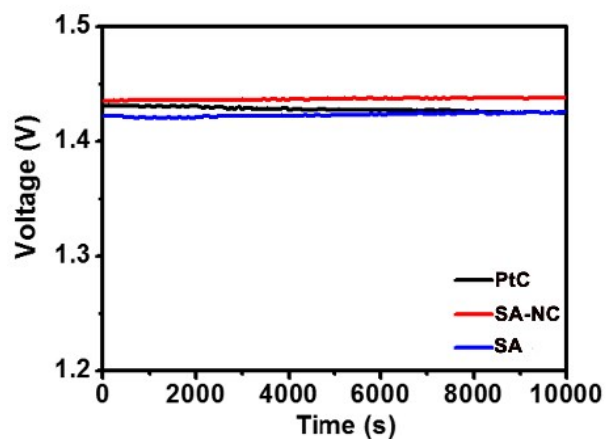
Table S1. Specific surface areas (SSA) and total pore volume (TPV) of carbon-based samples.

Samples	SSA ($m^2\ g^{-1}$)	TPV ($cm^3\ g^{-1}$)
N, S co-doped C_{PANI} catalysts	71.36	0.169
N, S co-doped $C_{PANI\text{ -TA}}$ catalysts	591.05	0.358
N, S co-doped $C_{PANI\text{ -Fe}}$ Fe-NP catalysts	251.18	0.414
N, S co-doped $C_{PANI\text{-TA-Fe}}$ Fe-SA-NC catalysts	599.07	0.57
N, S co-doped $C_{PANI\text{-TA-Fe}}$ Fe-SA catalysts	595.1	0.44

Table S2. The chemical compositions of N, S co-doped C$_{PANI-TA-Fe}$ Fe-NP catalysts, N, S co-doped C$_{PANI-TA-Fe}$ Fe-SA-NC catalysts, and N, S co-doped C$_{PANI-TA-Fe}$ Fe-SA catalysts obtained by EDS.

Samples	C (wt. %)	N (wt. %)	O (wt. %)	S (wt. %)	Fe (wt. %)
N, S co-doped C$_{PANI-TA-Fe}$ Fe-SA-NC catalysts	79.4	2.7	4.2	8.1	5.6
N, S co-doped C$_{PANI-Fe}$ Fe-NP catalysts	82.6	2.2	3.8	7.6	3.8
N, S co-doped C$_{PANI-TA-Fe}$ Fe-SA catalysts	82.15	2.4	6.6	7.9	0.95

Table S3. The chemical compositions of N, S co-doped $C_{PANI-TA-Fe}$ Fe-NP catalysts and N, S co-doped $C_{PANI-TA-Fe}$ Fe-SA-NC catalysts obtained by XPS.

Samples	C (wt. %)	N (wt. %)	O (wt. %)	S (wt. %)	Fe (wt. %)
N, S co-doped $C_{PANI-TA-Fe}$ Fe-SA-NC catalysts	75	4.3	8.6	7.5	4.6
N, S co-doped $C_{PANI-Fe}$ Fe-NP catalysts	77	2.8	13.9	4.3	2

Table S4. Relative quantity (at. %) of different C species from the deconvoluted peaks for C1s.

Samples	C sp^2 (at. %)	C sp^3 (at. %)	C-O & C-N & C-S (at. %)
N, S co-doped C$_{PANI-Fe}$ Fe-NP catalysts	48	31	21
N, S co-doped C$_{PANI -TA-Fe}$ Fe-SA-NC catalysts	58	26	16

Table S5. Relative quantity (at. %) of different N species from the deconvoluted peaks for N1s.

Samples	Pyridinic N (at. %) (398.4eV）	pyrrolic N (at. %) (400.4eV）	graphitic N (at. %) (401.2eV)	oxidized N (at. %) （403eV）
N, S co-doped C$_{PANI-TA-Fe}$ Fe-SA-NC catalysts	25.2	16.19	55.7	3
N, S co-doped C$_{PANI -Fe}$ Fe-NP catalysts	19.9	31.7	23.4	24.9

Table S6. Fe K-edge EXAFS curves Fitting Parameters.

sample	Scattering Pair	CN	R (Å)	σ^2 (10^{-3} Å^2)	ΔE_0 (eV)	R factor
FePC	Fe-N	4*	1.93	3.9	6.3	0.016
N, S co-doped C$_{PANI-TA-}$	Fe-N	4.1	2.05	6.6	-2.3	0.014
$_{Fe}$ Fe-SA-NC catalysts	Fe-O	1.9	1.92	6.6	0.162	

S_0^2 is the amplitude reduction factor and S_0^2 was fixed to 0.89; CN is the coordination number; R is interatomic distance (the bond length between central atoms and surrounding coordination atoms); σ^2 is DebyeWaller factor (a measure of thermal and static disorder in absorber-scatterer distances); ΔE_0 is edge-energy shift (the difference between the zero kinetic energy value of the sample and that of the theoretical model). R factor is used to value the goodness of the fitting.

Table S7. ORR performance of N, S co-doped C_{PANI} catalysts, N, S co-doped $C_{PANI-TA}$ catalysts, N, S co-doped $C_{PANI-Fe}$ Fe-NP catalysts, N, S co-doped $C_{PANI-TA-Fe}$ Fe-SA catalysts, N, S co-doped $C_{PANI-TA-Fe}$ Fe-NP catalysts, N, S co-doped $C_{PANI-TA-Fe}$ Fe-SA-NC catalysts and commercial Pt/C catalysts.

Samples	Onset potential (V vs. RHE)	Half potential (V vs. RHE)	Current density at 0.2 V (mA cm^{-2})
N, S co-doped C_{PANI} catalysts	0.87	0.78	3.8
N, S co-doped $C_{PANI-TA}$ catalysts	0.91	0.82	3.98
N, S co-doped $C_{PANI\ -Fe}$ Fe-NP catalysts	0.94	0.86	4.98
N, S co-doped $C_{PANI-TA-Fe}$ Fe-SA-NC catalysts	1.09	0.923	5.49
N, S co-doped $C_{PANI-TA-Fe}$ Fe-SA catalysts	1.04	0.89	5.01
N, S co-doped $C_{PANI-TA-Fe}$ Fe-NP catalysts	1.02	0.88	4.9
commercial Pt/C catalysts	0.99	0.88	5.2

Table S8. Half potentials (V vs. RHE) in 0.1 M KOH electrolyte of N, S co-doped $C_{PANI-TA-Fe}$ Fe-SA-NC catalysts and those reported in literature.

Catalysts	Half potential (V vs. RHE)	References
Fe_{SA}-N-C	0.891V	(7)
Fe-ZIF-8	0.78	(8)
Cu@Fe-N-C	0.892	(9)
Fe-ISA/SNC	0.896	(10)
FeN_x-PNC	0.86	(11)
Fe−N-DSC	0.8	(12)
ZIF'-FA-p	0.81	(13)
Fe-N-C-Phen-PANI	0.8	（14）
S,N-Fe/N/C-CNT	0.85	(15)
Fe-ISAs/CN	0.9	(16)
Fc@ZIF-8	0.904	(17)
N, S co-doped $C_{PANI-TA-Fe}$ Fe-SA-NC catalysts	0.923	This work

Table S9. Half potentials (V vs. RHE) in the acidic electrolyte of N, S co-doped $C_{PANI-TA-Fe}$ Fe-SA-NC-HT2 catalysts and those reported in literature.

Catalysts	Half potential (V vs. RHE)	References	electrolyte
Fe_{SA} -N-C	0.776	(6)	0.1 M $HClO_4$
Fe-N-C-950	0.78	(8)	0.1 M $HClO_4$
Cu@Fe-N-C	0.761	(9)	0.5 M H_2SO_4
Fe–N-DSC	0.712	(12)	0.5 M H_2SO_4
Fe@Aza-PON	0.541	(18)	0.1 M $HClO_4$
Fe-N-C	~0.73	(19)	0.1 M $HClO_4$
Co-N-C	0.8	(20)	0.1 M $HClO_4$
Co-N-C	0.73	(21)	0.1 M $HClO_4$
SA-Fe-N nanosheets	0.812	(22)	0.5 M H_2SO_4
f-FeCoNC900	0.8	(23)	0.1 M $HClO_4$
PNC-8	0.79	(24)	0.1 M $HClO_4$
NSC-1000	0.58	(25)	0.5 M H_2SO_4
N/Fe-CG	0.73	(26)	0.1 M $HClO_4$
NHC@G-900	0.65	(27)	0.5 M H_2SO_4
NDC-900-Fe	0.76	(28)	0.05 M H_2SO_4
N, S co-doped $C_{PANI-TA-Fe}$ Fe-SA-NC-HT2 catalysts	0.807	This work	0.1 M $HClO_4$

Table S10. Summary of the performances of Zn-air batteries reported in literature.

ORR Catalyst	Electrolyte	open-circuit potential (V)	peak power density (mW cm^{-2})	specific capacity (mAh g^{-1})	Reference
NSC-1000	6M KOH	1.47	167.8	634	(25)
HCSC-IV-H	6M KOH+0.2M Zn(CH$_3$OO)$_2$	1.430	104.9	593.6	(29)
(Zn,Co)/NSC	--	1.5	150		(30)
NOGB-800	6M KOH+0.2M Zn(CH$_3$OO)$_2$	1.50	111.9	--	(31)
CoNi/BCF	6M KOH+0.2M Zn(CH$_3$OO)$_2$	1.44	155.1	710.9	(32)
Fe-N$_x$-C	6M KOH+0.2M Zn(CH$_3$OO)$_2$	1.51	96.45	641	(33)
Zn-N-C-1	6M KOH	--	179	683.3	(34)
Ni–MnO/rGO	6M KOH+0.2M ZnCl$_2$	--	--	758	(35)
NPCS-900	6M KOH+0.2M Zn(CH$_3$OO)$_2$	--	79	684	(36)
Co-G@POF	6M KOH	--	78	--	(37)
N, S co-doped C$_{PANI-TA-Fe}$ Fe-SA-NC catalysts	6M KOH+0.2M Zn(CH$_3$OO)$_2$	1.44	136.4	795.1	This work

References

1 F. Jiao, A. Harrison, J. C. Jumas, A. V. Chadwick, W. Kockelmann and P. G. Bruce, *J. Am. Chem. Soc.*, 2006, **128**, 5468-5474.
2 M. Ma, H. Zhu, J. Ling, S. Gong, Y. Zhang, Y. Xia and Z. Tang, *ACS Nano* 2020, **14**, 4036-4044.
3 J. Herranz, F. Jaouen, M. Lefèvre, U. I. Kramm, E. Proietti, J. P. Dodelet, P. Bogdanoff, S. Fiechter, I. Abs-Wurmbach, P. Bertrand, T. M. Arruda and S. Mukerjee, *J. Phys. Chem. C*, 2011, **115**, 16087–16097.
4 X. Wang, D. Cullen, Y. Pan, S. Hwang, M. Wang, Z. Feng, J. Wang, M. Engelhard, H. Zhang, Y. He, Y. Shao, D. Su, K. More, J. Spendelow and G. Wu, *Adv. Mater.* 2018, **30**, 1706758.
5 G. Wan, P. Yu, H. Chen, J. Wen, C. Sun, H. Zhou, N. Zhang, Q. Li, W. Zhao, B. Xie, T. Li and J. Shi, *Small* 2018, **14**, 1704319.
6 B. C. Hu, Z. Y. Wu, S. Chu, H. W. Zhu, H. W. Liang, J. Zhang and S. H. Yu, *Energy Environ. Sci.*, 2018, 11, 2208–2215.
7 L. Jiao, G. Wan, R. Zhang, H. Zhou, S. H. Yu and H. L. Jiang, *Angew. Chem., Int. Ed.*, 2018, 57, 8525.
8 M. Xiao, J. Zhu, L. Ma, Z. Jin, J. Ge, X. Deng, Y. Hou, Q. He, J. Li, Q. Jia, S. Mukerjee, R. Yang, Z. Jiang, D. Su, C. Liu and W. Xing, *ACS Catal.*, 2018, 8, 2824–2832.
9 Z. Wang, H. Jin, T. Meng, K. Liao, W. Meng, J. Yang, D. He, Y. Xiong and S. Mu, *Adv. Funct. Mater.*, 2018, 28, 1802596.
10 Q. Li, W. Chen, H. Xiao, Y. Gong, Z. Li, L. Zheng, X. Zheng, W. Yan, W. C. Cheong, R. Shen, N. Fu, L. Gu, Z. Zhuang, C. Chen, D. Wang, Q. Peng, J. Li and Y. Li, *Adv. Mater.*, 2018, **30**, 1800588.
11 L. Ma, S. Chen, Z. Pei, Y. Huang, G. Liang, F. Mo, Q. Yang, J. Su, Y. Gao, J. A. Zapien and C. Zhi, *ACS Nano*, 2018, **12**, 1949.
12 Z. Huang, H. Pan, W. Yang, H. Zhou, N. Gao, C. Fu, S. Li, H. Li and Y. Kuang, *ACS Nano*, 2018, **12**, 208–216.
13 C. Zhang, Y. C. Wang, B. An, R. Huang, C. Wang, Z. Zhou and W. Lin, *Adv. Mater.*, 2017, **29**, 1604556.
14 X. Fu, P. Zamani, J. Y. Choi, F. M. Hassan, G. Jiang, D. C. Higgins, Y. Zhang, M. A. Hoque and Z. Chen, *Adv. Mater.*, 2017, **29**, 1604456.
15 P. Chen, T. Zhou, L. Xing, K. Xu, Y. Tong, H. Xie, L. Zhang, W. Yan, W. Chu, C. Wu and Y. Xie, *Angew. Chem., Int. Ed.*, 2017, **56**, 610–614.
16 Y. Chen, S. Ji, Y. Wang, J. Dong, W. Chen, Z. Li, R. Shen, L. Zheng, Z. Zhuang, D. Wang and Y. Li, *Angew. Chem., Int. Ed.*, 2017, **56**, 6937–6941.
17 J. Wang, G. Han, L. Wang, L. Du, G. Chen, Y. Gao, Y. Ma, C. Du, X. Cheng, P. Zuo and G. Yin, *Small*, 2018, **14**, 1704282.
18 S. J. Kim, J. Mahmood, C. Kim, G. F. Han, S. W. Kim, S. M. Jung, G. Zhu, J. J. De Yoreo, G. Kim and J. B. Baek, *J. Am. Chem. Soc.*, 2018, **140**, 1737–1742.
19 J. Yi, R. Xu, Q. Wu, T. Zhang, K. Zang, J. Luo, Y. Liang, Y. Huang, R. Cao, *ACS Energy Lett.,* 2018, **3**, 883-889.
20 X. Wang, D. Cullen, Y. Pan, S. Hwang, M. Wang, Z. Feng, J. Wang, M. Engelhard, H. Zhang, Y. He, Y. Shao, D. Su, K. More, J. Spendelow, G. Wu, *Adv. Mater.,* 2018, **30**, 1706758.
21 G. Wan, P. Yu, H. Chen, J. Wen, C. Sun, H. Zhou, N. Zhang, Q. Li, W. Zhao, B. Xie, T. Li, J. Shi, *Small,* 2018, **14**, 1704319.
22 Z. Miao, X. Wang, M. C. Tsai, Q. Jin, J. Liang, F. Ma, T. Wang, S. Zheng, B. J. Hwang and Y. Huang, *Adv. Energy Mater.*, 2018, **8**, 1801226.
23 G. Zhang, Y. Jia, C. Zhang, X. Xiong, K. Sun, R. Chen, W. Chen, Y. Kuang, L. Zheng, H. Tang, W. Liu, J. Liu, X. Sun, Wen. Lin, H. Daie, *Energy Environ. Sci.*, 2019, **12**, 1317-1325.
24 T. Najam, S. S. A.Shah, W. Ding, J. Jiang, L. Jia, W. Yao, L. Li, Z. Wei, *Angew. Chem., Int. Ed.,* 2018, **57**, 15101.
25 K. Yuan, C. Lu, S. Sfaelou, X. Liao, X. Zhuang, Y. Chen, U. Scherf, X. Feng, *Nano Energy,* 2019, **59**, 207–215.
26 B. Li, S. P. Sasikala, D. H. Kim, J. Bak, I. D. Kim, E. Cho, S. O. Kim, *Nano Energy,* 2019, **56**, 524–530.
27 J. Q. Sun, S. E. Lowe, L. J. Zhang, Y. Z. Wang, K. L. Pang, Y. Wang, Y. L. Zhong, P. R. Liu, K. Zhao, Z. Y. Tang, H. J. Zhao, *Angew. Chem. Int. Ed.,* 2018, **57**, 16511– 16515.
28 A. Mehmood, J. Pampel, G. Ali, H. Y. Ha, F. Ruiz-Zepeda, T. P. Fellinger, *Adv. Energy Mater.,* 2018, **8**, 1701771.
29 W. Yang, Y. Zhang, X. Liu, L. Chen, M. Liu, J. Jia, *Carbon*, 2019, **147**, 83-89.
30 D. Liu, B. Wang, H. Li, S. Huang, M. Liu, J. Wang, Q. Wang, J. Zhang, Y. Zhao, *Nano Energy*, 2019, **58**, 277-283.
31 Q. Hu, G. Li, G. Li, X. Liu, B. Zhu, X. Chai, Q. Zhang, J. Liu, C. He, *Adv. Energy Mater.,* 2019, **9**, 1803867.
32 W. Wan, X. Liu, H. Li, X. Peng, D. Xi and J. Luo, *Appl. Catal., B*, 2019, **240**, 193–200。
33 J. Han, X. Meng, L. Lu, J. Bian, Z. Li, C. Sun, *Adv. Funct. Mater.*, 2019, 1808872.
34 J. Li, S. Chen, N. Yang, M. Deng, S. Ibraheem, J. Deng, J. Li, *Angew. Chem. Int. Ed.,* 2019, **58**, 1-6.
35 G. Fu, X. Yan, Y. Chen, L. Xu, D. Sun, J. M. Lee and Y. Tang, *Adv. Mater.*, 2018, **30**, 1704609.
36 S. Chen, L. Zhao, J. Ma, Y. Wang, L. Dai, J. Zhang, *Nano Energy*, 2019, **60**, 536-544.
37 B. Li, C. Zhao, S. Chen, J. Liu, X. Chen, L. Song, Q. Zhang, *Adv. Mater.,* 2019, 1900592.